ROYAL SOCIETY OF CHEMISTRY

PAPER

Check for updates

Impact on silica particle physical characteristics of co-condensed alkoxide precursors†

Francisco Bevilacqua,[a] Cynthia Cibaka-Ndaya,[a] Paula Sanz Camacho,[a] Sabrina Lacomme,[b] Etienne Durand,[a] Jean-Bernard Ledeuil,[c] Joachim Allouche, [iD][c] Cédric Boissière, [iD][d] Clément Sanchez [iD]*[d] and Glenna L. Drisko [iD]*[a]

Understanding the condensation process of two precursors in the Stöber process is crucial to enhance the complexity and applicability of silica hybrids. We present a simple and effective method to prepare functional silica hybrid particles with tunable properties through the co-condensation of tetraethoxysilane and an organoalkoxide precursor using a modified Stöber process. Three organoalkoxide precursors have been studied: (3-mercaptopropyl)triethoxysilane, (3-cyanopropyl)triethoxysilane, and (3-aminopropyl)triethoxysilane. All three investigated systems produce functional silica hybrid particles, as confirmed by various characterization techniques. Scanning transmission electron microscopy and nitrogen sorption analysis demonstrated that features such as the microstructure could be tailored by the careful selection of the second precursor. A drastic increase in the specific surface area can be obtained with 3cyanopropyltriethoxysilane: 270 m^2 g^{-1} compared to 17 m^2 g^{-1} in the unfunctionalized silica particles. Other important characteristics such as the degree of condensation and surface charge can also be influenced by precursor choice. The enhanced reactivity of 3-aminopropyltriethoxysilane yields a higher degree of particle functionalization. Nanoscale chemical mapping has been performed using energy-dispersive Xray spectroscopy and Auger spectroscopy. Homogeneous distribution of the functionalities within the hybrid particles occurs. The present work gives tools to easily tailor functional silica particles, thus providing simple ways to tune their properties to meet a wide range of applications.

Introduction

Silica particles and silica hybrid particles are materials used in various fields, including biomedicine,[1] photonics,[2] and as resonant units in metamaterials.[3,4] Although the Stöber synthesis was developed in 1968 and heavily researched since,[5–8] there is still mystery around how particle aggregation occurs when organically modified precursors are added into the synthetic pot. This is because of the multiple processes occurring in sol–gel chemistry: precursor hydrolysis, condensation and redissolution, the kinetics of seed particle nucleation and growth, the process of seed particle aggregation, and Ostwald ripening. These processes are impacted by the specifics of the reaction, such as the influence of the selected precursor, and synthetic conditions, for instance, relative

concentrations, temperature, and stirring rate. Understanding how organically modified silicon alkoxide precursors impact particle formation, in terms of porosity, surface potential, size and shape, is therefore needed to increase the quality and applicability of hybrid silica particles. It is known that hydrolysis is the rate-limiting step in Stöber reactions.[9] Due to precursor accessibility, functionalized silica particles are mainly prepared using organoalkoxide precursors. For instance, (3-aminopropyl)triethoxysilane (APTES) is commonly used in applications such as coatings, adhesives, and chromatography.[10] (3-Mercaptopropyl)triethoxysilane (MPTES) is used for grafting gold onto silica surfaces, and inversely to coat gold with silica.[11] (3-Cyanopropyl)triethoxysilane (CPTES) can be used in liquid chromatography as a hydrophobic coating, but also opens possibilities to further functionalize the silica surface using click chemistry to attach complex molecules.[7]

Some protocols exist that use only organosilanes to make colloids. In particular, MPTES and CPTES have been studied. It has been shown that they could be used to produce large particles with relatively broad size distribution.[12] To the best of our knowledge, APTES alone cannot form particles, but it has been co-condensed with TEOS.[12–14] There are a limited number of studies of tandem precursor co-condensation[5,8,15–20] Most commonly, the second precursor is added *via* a second step

[a] *Univ. Bordeaux, CNRS, Bordeaux INP, ICMCB, UMR 5026, F 33600 Pessac, France. E-mail: glenna.drisko@ens-lyon.fr*

[b] *Univ. Bordeaux, CNRS, INSERM, BIC, UAR 3420, F-33600 Pessac, France*

[c] *Univ. Pau et des Pays de l'Adour, E2S UPPA, IPREM/CNRS, UMR 5254, 64000 Pau, France*

[d] *Laboratoire Chimie de la Matière Condensée, UMR UPMC Collège de France-CNRS 7574, Paris, France*

† Electronic supplementary information (ESI) available. See DOI: https://doi.org/10.1039/d4tc04305g

after an already advanced degree of TEOS condensation, to ensure the presence of functionalities at the surface of the silica particles.[5,10,21,22] However, there is value in studying co-condensed systems. One precursor may catalyze the condensation of the other, or contrarily, may inhibit the reaction. In addition to the change in chemical functionality, mixing two precursors simultaneously might change the physical properties of the produced objects. Kurdyukov et al. co-condensed TEOS and an organoalkoxide with a methacrylic functionality via Stöber, showing that they could increase particle porosity by changing the relative quantity of the second precursor.[5] Co-condensation of APTES and TEOS has been studied by Van Blaaderen et al., observing an increase in microporosity and a decrease in the degree of siloxane condensation compared to the pure TEOS system.[10] However, when APTES was added in a second step, the degree of condensation on the surface of pure silica particles increased, as observed through the disappearance of Q^2 entities in the ^{29}Si NMR and a slight reduction in the quantity of Q^3.[10] Lin et al.[8] prepared co-condensed vinyltriethoxysilane and TEOS and reported the used vinyltriethoxysilane as a size-tuning agent, increasing the monodispersity of their samples. The vinyltriethoxysilane precursor was added after silica nucleation, to ensure surface functionalization of the particles. It was shown that an increase in the mol% of the second precursor decreased the particle size, preventing Ostwald ripening and particle growth.

The degree of incorporation of organosilanes into the silica structure depends on the kinetics of precursor hydrolysis and condensation, where it is possible that the organoalkoxide precursor impacts the reactivity of TEOS.[23–26] In studies on the hydrolysis rate of different organic precursors, it has been found that APTES tends to catalyse this step, under neutral conditions.[24] In alkaline conditions, the condensation is so favourable that a 3D network rapidly forms, complicating the analysis of the APTES system.[24,27] MPTES was also part of this study, showing a lower reactivity than APTES. To our knowledge no systematic study exists of co-condensed TEOS and CPTES, or similar molecules.

To date, no one has assessed the spatial distribution of elemental composition at the nanoscale in a co-condensed two-precursor system. Only a microscale characterization has been reported, showing the presence of different functional groups within a particle.[18] In the design of sol–gel materials, the use of different precursors might affect the spatial distribution of the functional groups generating interfaces that influence material properties. A better characterization of elemental distribution at the nanoscale, and of the organic–inorganic interfaces in hybrid materials, is crucial to develop advanced nanostructured materials with complex and tailored functionality and morphology.

In this work, we propose an extensive study of three different co-condensed systems prepared in a one-step synthesis. Fundamental differences are observed within the prepared objects. We confirm some previously observed trends and also show the efficiency of this method in the preparation of functional materials with tailored properties, depending on the selected organoalkoxide precursor. The nature of the organoalkoxide precursor impacts particle size, shape, porosity, and polydispersity within a batch. Nitrogen sorption analysis shows that the particles exhibit highly different surface aspects. The particles containing thiol and cyano functional groups show a higher specific surface area and a higher quantity of microporosity than the pure TEOS system. We observe that the amine functionality, in our case, tends to decrease the microporosity of the particles, compared to pure silica. TGA analysis demonstrated differences in the incorporation of the functional group depending on the precursor used, and NMR analysis was consistent with an influence of the second precursor on the particles' degree of condensation. We demonstrate a relationship between the degree of condensation and the microstructure of the objects produced. We have performed chemical mapping of the particles using Auger spectroscopy to assess the distribution of functionality at the nanoscale. We show that the co-precipitation of TEOS and another precursor does not create a gradient of composition, as might be expected due to differences in hydrolysis and condensation kinetics, but instead results in a homogeneous distribution of functionalities throughout the particles, explained by particle growth via seed particle aggregation.

Experimental section

Materials

Tetraethyl orthosilicate ($\geq$99.0%, 86578), ammonium hydroxide solution (29%, 221228), (3-aminopropyl)triethoxysilane ($\geq$99.0%, 440140), (3-mercaptopropyl)triethoxysilane ($\geq$80%, 63797), (3-cyanopropyl)triethoxysilane ($\geq$98%, 374156), and the buffer solution used for the zeta potential measurement (potassium dihydrogen phosphate/di-sodium hydrogen phosphate, 12161706) were purchased from Sigma Aldrich. Ethanol (EtOH, 99.9%, PC80101.9200) was supplied by Atlantic Labo. Carbon/copper grids were obtained from Delta Microscopies. All chemicals were used without further purification. Aqueous solutions were prepared using deionized water, obtained from a Type 1 Milli-Q water purification system (18.2 MΩ cm).

Synthesis of SiO$_2$ particles

Functionalized silica particles were prepared by adapting a protocol by Gao et al.[2] To a 250 mL round bottom flask, ethanol (104 mL) and ultrapure water (3 mL) were added. The flask was immersed in a 60 °C oil bath for at least 30 min under magnetic stirring, to reach the reaction temperature. An ammonium hydroxide solution (10 mL, 29% v/v) was then added to the solution, yielding a pH ∼ 10.5. Subsequently, a freshly prepared solution containing a mixture of TEOS and the organoalkoxide was added under vigorous stirring. Three different ratios of TEOS/organosilane mol% have been studied: 90/10, 80/20, and 70/30 mol%. The volumes used for the different molar ratios are presented in Table 1. A suspension of silica particles formed after 5–10 min. A precipitate did not form until the sample was centrifuged; at which time a pellet was formed at the base of the centrifuge tube. After 2 h of reaction, the particles were removed from the oil bath and centrifuged at a g-force of 6654

This journal is © The Royal Society of Chemistry 2025

J. Mater. Chem. C, 2025, **13**, 7318–7326 | 7319

Table 1 Used volumes of precursors depending on the molar ratio. Molar fraction (TEOS/precursor)

	100	90/10	80/20	70/30
V_{TEOS} (mL)	6	5.4	4.8	4.2
$V_{4-CPTES}$ (mL)	0	0.65	1.3	1.95
$V_{3-MPTES}$ (mL)	0	0.803	1.60	2.41
$V_{3-APTES}$ (mL)	0	0.635	1.27	1.90

for 30 min before being redispersed in a small volume of ethanol. In the case of the MPTES precursor at concentrations of 20, and 30 mol%, the solution must be centrifuged directly after 2 h of reaction to avoid macroscopic gelation, thus all samples were treated as such.

Characterization

Transmision electron microscopy (TEM). To prepare samples for analysis, a few droplets of particles suspended in ethanol were dropcasted over grids composed of a carbon film-coated 300 mesh square copper lattice. Particles were imaged using either a JEOL 1400F TEM using a 120 kV acceleration voltage or a Hitachi H7650 with an acceleration voltage of 80 to 120 kV in high-resolution mode. All TEM images were acquired with the Gatan software Digital Micrograph.

Scanning transmission electron microscopy/energy dispersive X-ray spectroscopy (STEM/X-EDS). Grids were examined with a transmission electron microscope (Talos F200S G2 FEG – Thermofisher – Eindhoven) at 200 kV, equipped with a 4K*4K camera One View (Gatan, Paris (France)). For STEM/X-EDS mode, the operational parameters were a condenser aperture C2 of 70 μm (converge angle of 10.5 mrad), a current around 0.415 nA, a spot size of 6, a camera length of 260 mm (HAADF: 29–177 mrad) to optimize the spatial resolution and X photons rate (around 500 to 1 K counts per s – 1% dead time). The STEM pictures and X-EDS spectra and maps were collected using Velox software (Thermofisher company).

The TEM/STEM images and the spectra/elemental maps have been converted to tiff or jpg format after their treatment in Velox.

Auger electron spectroscopy (AES) and scanning Auger mapping (SAM). The experiments were carried out with a JEOL JAMP 9500F Auger Microprobe spectrometer (JEOL Ltd, Tokyo, Japan) working under ultrahigh vacuum conditions (pressure $< 2 \times 10^{-7}$ Pa). The spectrometer was equipped with a Schottky field emission electron gun leading to very high spatial resolution analysis and high brightness. The hemispherical electron analyzer coupled with a multichannel detector (7 channeltrons) offered ideal settings for high throughput analysis and variable energy-resolved Auger analysis. Scanning electron microscopy (SEM) images, SAM images, and Auger spectra were recorded using an acceleration voltage of 10 keV, a probe current of 3 nA, and a working distance of 23 mm (sample tilt angle = 45°). Spectra (kinetic energy from 0 to 600 eV) were carried out in constant retarding ratio mode with $\Delta E/E = 0.5\%$ (high sensitivity). The SAM images were performed in constant analyzer energy operating conditions to define the useful energy width needed to

obtain a significant peak background-intensity difference concerning the Auger transition and the background shape. An auto probe tracking correction was also used to control and compensate for the drift, due to the balance of sample surface charge effects and instrument-dependent fluctuations.

For Auger analyses, the particles were dispersed in ethanol at a concentration of 10 mg L^{-1}. Four drops of the dispersion were then deposited on a small silicon wafer through several cycles of one droplet deposition-solvent evaporation at room temperature. The silicon wafer was finally polished using an Ar$^+$ ion beam in a cross-section polisher (model IB-09010CP, Jeol Ltd., Tokyo, Japan) operating at 5 keV for 2 h (working pressure of 1×10^{-4} Pa). The edge cut was then observed and analyzed in the Auger electron nanoprobe using a cross-cut section sample holder.

Nitrogen adsorption–desorption analysis. Before nitrogen sorption analysis, the particles were centrifuged twice at 6000 rpm for 30 min and dried in an oven at 70 °C. The surface area and pore sizes of the prepared materials were determined using nitrogen physisorption with a Micromeritics 3Flex analyzer. The samples were degassed at 150 °C and 50 mTorr overnight before analysis. The surface area was calculated using the multipoint BET (Brunauer–Emmett–Teller) method. The *t*-plot method was used to access the volume of micropores, following the De Boer equation.[28]

Zeta potential. To evaluate the particle surface charge, zeta potential values of the particle surfaces were measured using laser Doppler electrophoresis with a Wallis zeta potential analyzer from Cordouan Technologies®. The particles were centrifuged and dispersed in a buffer solution at pH 7 prior to measurement. The particles were then aged in solution for 10 min. Six measurements of the zeta potential of the sample were performed and averaged.

Solid-state nuclear magnetic resonance (NMR) spectroscopy. Solid-state NMR spectra were recorded by using Bruker Avance III spectrometers equipped with 7.05T wide-bore superconducting magnets corresponding to a ^{29}Si Larmor frequency of 59.6 MHz. All data were acquired using a 4 mm double-resonance Bruker MAS NMR probe, with a magic angle spinning (MAS) rate of 10 KHz. Chemical shifts are referenced relative to silicon oil at −22 ppm, used as a secondary reference.

Direct excitation ^{29}Si MAS experiments were acquired using a short pulse length of 3 μs corresponding to a selective π/2 pulse determined by silicon oil. Spectra were acquired with 3072 transients separated by cycle intervals of 60 s. Although T1 is very long for all ^{29}Si resonances, there is little difference in the relative relaxation rates, and spectral intensities accurately reflect the relative site populations at 60 s. Cross polarization (CP) ^{29}Si MAS NMR data were acquired from ^{1}H using a square contact pulse of 3 ms and ^{1}H decoupling (TPPM) during acquisition. Spectra were acquired with between 4096–5200 transients separated by cycle intervals of 3 s. Deconvolution of the ^{29}Si MAS NMR spectra was performed using the DmFIT program.

Thermogravimetric analysis (TGA). TGA was performed on a Setaram Setsys Evo, increasing the temperature from 25 to 800 °C at 10 °C min^{-1}, under an air flow of high purity air

7320 | *J. Mater. Chem. C*, 2025, **13**, 7318–7326

This journal is © The Royal Society of Chemistry 2025

Paper

(Air Liquide 5.0) at 50 mL min^{-1}. A platinum crucible was used for the experiments.

Results and discussion

The procedure used to prepare the hybrid silica particles is based on a protocol reported by Gao et al.[2] and schematically represented in Fig. 1. The average particle size can be easily adapted using this protocol by simply modifying the volume of ethanol in the reaction flask. Moreover, this procedure is reported as highly reproducible, which is in agreement with our preliminary experiments (Fig. S1, ESI†).

The method used efficiently produces particles. The size of the particles and their dispersity can be found in Table S1 (ESI†). We observe that most of the prepared samples exhibit a relatively low size dispersion (<10% Table S1, ESI†). Other samples displayed bimodal distribution with two discrete sizes with narrow size dispersity. At 10 mol% TEOS substitution with the different organoalkoxides, we can observe differences in particle dispersity and shape (Fig. 2a–c). The particles prepared with 10 mol% of CPTES and MPTES (Fig. 2a and b, respectively) are quite similar in shape to the pure silica particles, and show a satisfying size distribution (Fig. S2 and Table S1, ESI†). However, in Fig. 2c, we see a clear impact on the shape of the particles with 10 mol% APTES, which also display a larger size distribution (Table S1, ESI†). The particles prepared with 30 mol% organoalkoxide are presented in Fig. 2d–f. The entities synthesized with CPTES and MPTES kept the spherical shape observed for pure TEOS particles, but exhibit a high secondary population of particles. Regarding the APTES hybrids, we see in Fig. 2f that the deformation observed at 10 mol% is further enhanced as the quantity of APTES is increased.

Such particle shape deformation was previously observed by Van Blaaderen et al. in their work on similar objects.[10] The deformations do not appear to be induced by shearing of the solution, otherwise we would also have deformation in the particles formed from pure TEOS and the other co-condensed systems. The deformation observed is therefore likely due to aggregation followed by growth at an intermediate stage in the growth of the particles. In order to observe this phenomenon, the growing particles need to be able to approach each other and interact. The introduction of ammonium and amine functions is likely to produce this effect by increasing chemical

reactivity through nucleophilic catalysis, whereas the presence of the other, hydrophobic functions does not favour the formation of hydrogen or covalent bonding. This effect is compatible with the observation that this sample does not show bimodal particle sizes (Table S1, ESI†). Both the rate of particle generation and the surface chemistry impact the formation of larger particles formed through an aggregation mechanism.[29] It is possible that the surface chemistry of the seed particles changes with time due to differences in the hydrolysis and condensation rates of TEOS, APTES, CPTES and MPTES. However, we have not been able to isolate the smaller particles to characterize differences between large and small particles within a batch.

The TGA analysis displayed in Fig. 2g shows differences in the total weight loss of the different systems, which are associated with the incorporation of the organic functionality within the particles. To interpret the TGA results, a correction must be made, associated with the loss of solvent within the material. The mass at 150 °C is considered to be the dried mass of the particles after the loss of surface bound water and solvent. Surprisingly, the amine functionalized particles lose the lowest mass of water, compared to the other systems, despite its hydrophilicity, while the hydrophobic cyano function displays the highest weight losses below 150 °C. We assume that this is due to the impact of the relative surface area on the quantity of physisorbed water. From the thermal analysis, a higher incorporation of the amine functionality within the material is observed (7 wt%), followed by the thiol (3.7 wt%) and cyano (1.6 wt%). The shoulder starting around 250 °C, is associated with the condensation of hydroxyl groups.[30] Differences in the mass loss at these two temperatures show that the particles exhibit differences in water adsorption and the degree of condensation. The APTES-prepared particles exhibit a more complex decomposition profile with an almost steady weight loss up to 750 °C. Similar behaviour is observed in the literature and is associated with the decomposition of the amine functionality.[31,32] APTES was integrated into the particles to a greater degree than CPTES and MPTES, probably due to its greater reactivity and much greater affinity to the forming hydrophilic silicate network.

Zeta potential measurements reflect the electrical potential in the vicinity of the particle surface in solution, thus this parameter depends on the chemical structure and density of functional groups on the particle surface. The observed zeta potential value for silica is similar to what is observed in the literature.[33] The three hybrid systems exhibit differences in their zeta potential values (Fig. 2h). We attribute these differences to the presence of the different organic moieties at the particle surface and to different quantities of silanols. The cyano functionalization has a surface potential similar to the 100 mol% TEOS system. A small decrease is observed, probably due to electronic effects from the cyano group stabilizing the formation of Si–O^{-}. Other functionalized particles show a stronger influence on the zeta measurement. The thiol-functionalized particles have the lowest potential, and the APTES-prepared particles have the highest, as has been
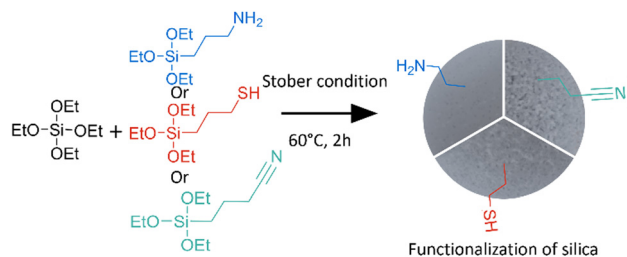

Fig. 1 Schematic representation of the synthetic approach to prepare hybrid silica particles, by combining TEOS with APTES, MPTES or CPTES to create organofunctionalized silica particles.

This journal is © The Royal Society of Chemistry 2025

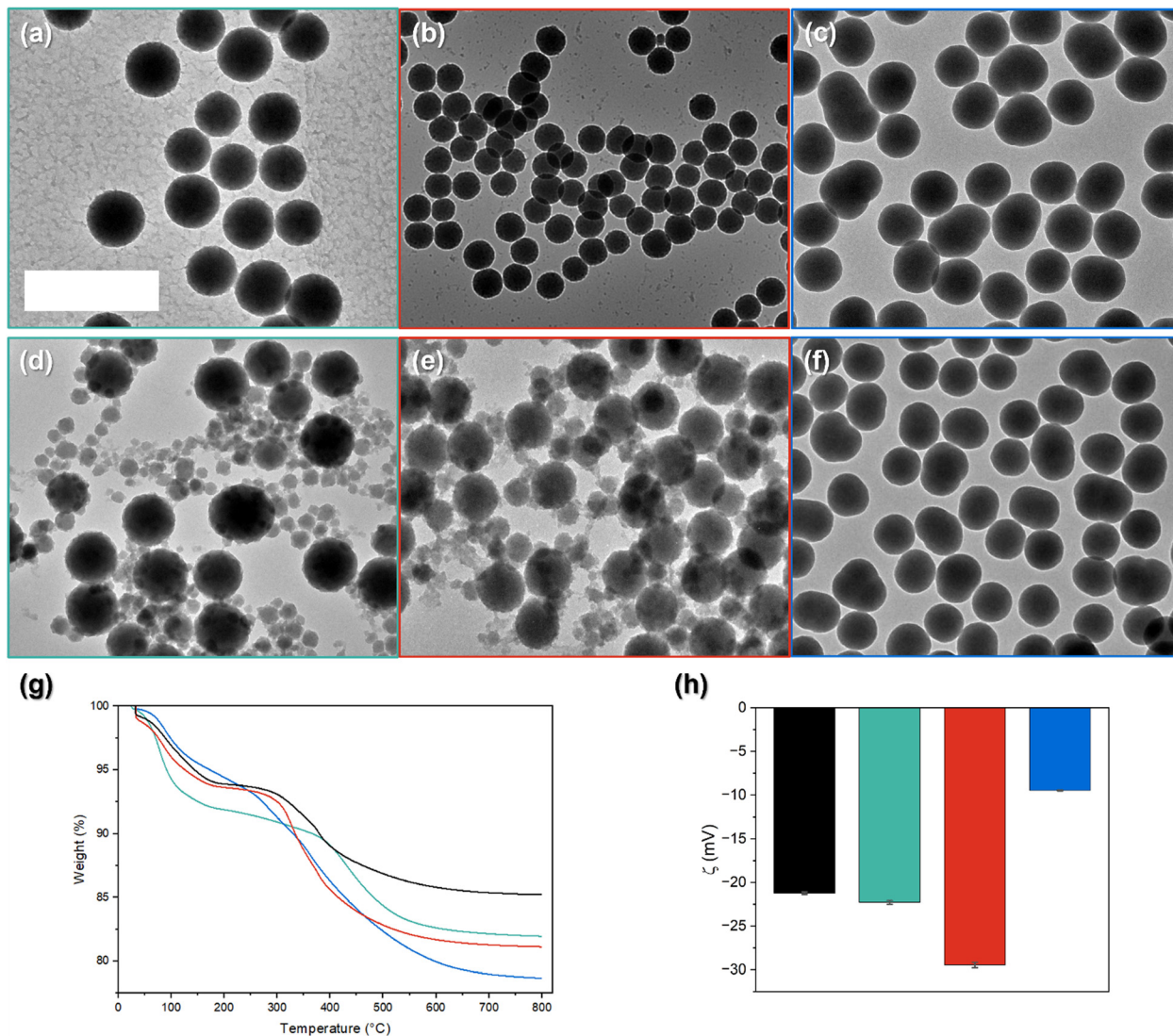J. Mater. Chem. C, 2025, **13**, 7318–7326 | 7321

Fig. 2 Micrographs of particles prepared using TEOS and either (a)–(c) 10 or (d)–(f) 30 mol% of (a) and (d) CPTES, (b) and (e) MPTES, or (c) and (f) APTES. Scale bars represent 500 nm. (g) TGA and (h) measured Zeta potential of the four systems: silica (black), and the hybrids CPTES (green), MPTES (red), and APTES (blue) prepared with 70/30 mol%.

observed previously.[21] This is a consequence of their acid–base behavior. Regarding the APTES-prepared systems, the surface potential suggests a higher quantity of Si–O$^-$ on the particle surface than –NH^{3+} groups. Positive zeta potentials have been observed in the literature for the post-synthetic functionalization with APTES.[21,34] We explain this difference as a consequence of post-surface functionalization decreasing the quantity of uncondensed silanols, which does not occur in the case of co-condensed APTES and TEOS. The quantity of silanols on the surface can even increase upon co-condensation, which will be shown to be the case in the NMR characterization. For the cyano- and thiol-functionalized particles, the zeta potential is a balance between the degree of silanols present on the surface and the change in surface charge upon incorporation of the functional groups.

STEM images presented in Fig. 3a–c give information about surface morphology differences among the three hybrid systems. Similarly to what is observed in the TEM micrographs (Fig. 2d and e), the cyano- and thiol-functionalized particles exhibit similarities in their surface roughness. This is in opposition to the amine-functionalized particles, which present a smooth surface. These differences in surface roughness are emphasized by the specific surface area retrieved by nitrogen sorption analysis in each case.

Fig. 3(d and e) presents the sorption isotherm and the t-plots of the different systems. The particles with the highest specific surface area are the particles prepared with the cyano-functionalized precursor with $\sim$270 m^2 g^{-1}, followed by the thiol-functionalized with $\sim$75 m^2 g^{-1} and then the amine-functionalized with $\sim$33 m^2 g^{-1}. The particles prepared with pure TEOS exhibit a lower specific surface area value of $\sim$17 m^2 g^{-1}. The higher specific surface area of cyano- and thiol-functionalized particles is consistent with their rougher appearance, which appears to provide more

7322 | J. Mater. Chem. C, 2025, 13, 7318–7326

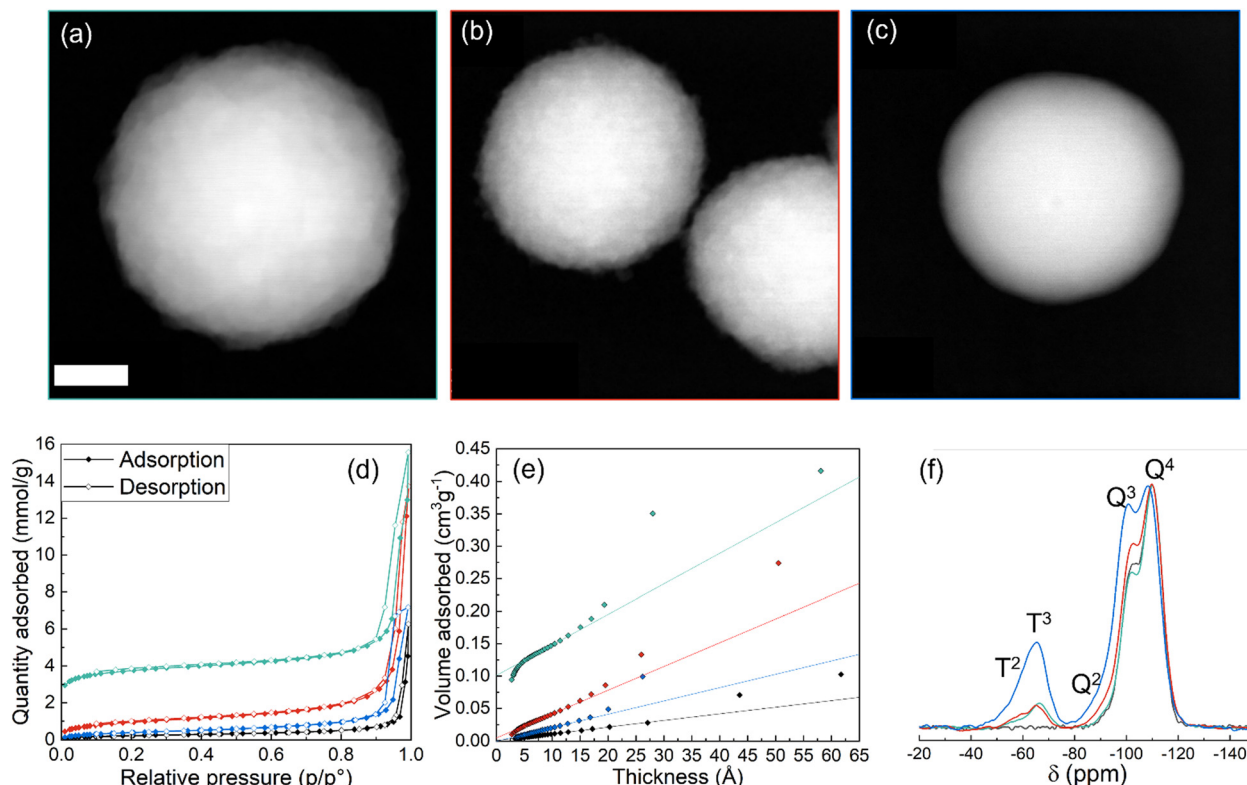This journal is © The Royal Society of Chemistry 2025

Fig. 3 Internal meso- and micropore structure and degree of silica condensation. STEM micrographs of the particles prepared with 70 mol% TEOS and 30 mol% of (a) CPTES, (b) MPTES, and (c) APTES. The scale is equivalent, with the scale bar representing 50 nm. (d) Nitrogen sorption isotherms and (e) their associated t-plots. (f) ^{29}Si MAS NMR spectra of the particles prepared with TEOS (black), and a 70/30 mol% of TEOS/CPTES (green), MPTES (red), and APTES (blue), normalized to the Q^4 signal for better comparison.

nitrogen adsorption sites on the particles. This likely results from the lower propensity of the seed particles to re-dissolve, condense and ripen after aggregation. Regarding maximum adsorption, the same hierarchy is observed among the four systems. The t-plot analysis permits an estimation of the micropore volume in the material. From these experiments, we observed that the cyano-functionalized particles show the highest microporosity (~ 0.1 cm^3 g^{-1}), and that the particles functionalized with amine do not exhibit any microporosity. The microporosity variations among the hybrids are consistent with their differences in specific surface area. The pure TEOS system exhibits almost no microporosity, which is unusual for TEOS particles produced using a Stöber synthesis. Higher values of micro- and mesoporosity are usually reported in the literature.[35] The microporosity of Stöber particles has been explained to result from the incomplete condensation of TEOS.[28] We thus report that the protocol developed by Gao et al.,[2] where the sol–gel reaction occurs at 60 °C, produces densified silica particles compared to room temperature Stöber processes. The analyses presented here show that a careful choice of precursor is a suitable tool to finely control the specific surface area and microporosity of the final hybrid particles, which is of high importance for numerous applications. For instance, the higher specific surface area in the cyano-functionalized particles may make these particles favorable for further click chemistry functionalization.

^{29}Si MAS NMR spectroscopy is performed to better understand the differences observed in the microporosity and to have insight

into differences in precursor reactivity. ^{29}Si MAS NMR analysis differentiates between quaternary and ternary systems.[21] Quaternary entities (Q^n), characterized in Fig. 3f by displacement around -100 ppm, are signals of silicon tetrahedrons surrounded by 4 oxygen atoms, where n defines the number of oxygen bridges between silicon atoms. Similarly, ternary systems (T^n) define silicon surrounded by 3 oxygen atoms such as SiO$_3$R, with n the number of oxygen bridges between silicon atoms. The presence of Q^4 and Q^3 are identified in each of the studied systems, and appear around -110 and -100 ppm respectively (Table S1, ESI†). Fig. 3f shows the direct excitation ^{29}Si MAS NMR spectra of all materials, normalized to the Q^4 at -110 ppm to facilitate the comparison within the hybrids. We quantitatively compare the systems by using the degree of condensation of the quaternary and ternary systems, coupled with the relative percentage of the different Q^n and T^n entities. The different percentages were obtained from a deconvolution fitting of the ^{29}Si MAS NMR spectra (Fig. S4, ESI†). The degree of condensation is calculated following eqn (1) and (2);

$$c(Q) = \frac{4 \times Q^4(\%) + 3 \times Q^3(\%) + 2 \times Q^2(\%) + Q^1(\%)}{4} \quad (1)$$

$$c(T) = \frac{3 \times T^3(\%) + 2 \times T^2(\%) + T^1(\%)}{3} \quad (2)$$

With $c(Q)$ the degree of condensation of Q^n entities and $c(T)$ the degree of condensation of T^n (Table S1, ESI†). The degree of

Table 2 Relative percentage of the Q^n signals, and T^m signals for the pure TEOS and the hybrid system at 70/30 mol% TEOS/organoalkoxide

	Q^2 (%)	Q^3 (%)	Q^4 (%)	T^2 (%)	T^3 (%)
TEOS	1	42	57		
TEOS-APTES	0	45	55	35	65
TEOS-CPTES	2	35	63	34	66
TEOS-MPTES	3	43	55	45	55

condensation was essentially equivalent for all four of the samples. We think it is more relevant to discuss the relative values of each of the component. For instance, non-

functionalized, silica particles only show Q^n signal consisting mainly of Q^3 ($\sim$42%), and Q^4 ($\sim$57%) moieties. According to deconvolution fitting, there is a small contribution of Q^2 up to 1%. However, ^{29}Si CP did not depict a noticeable peak, which suggests a negligible presence of Q^2 in this system (Fig. S4, ESI†). In the MPTES and CPTES we observe a relatively similar percentage of Q^2 containing $\sim$3%, and $\sim$2% respectively, while APTES particles did not show any Q^2 (Table 2 and Fig. S5, ESI†). The Q^3 and Q^4 are essentially the same for all samples except for CPTES, which shows a decrease in Q^3 (Fig. 3 and Table 2). As expected, the ternary systems (T) are only present in the hybrid systems, and only T^3 and T^2 are found (Fig. 3 and
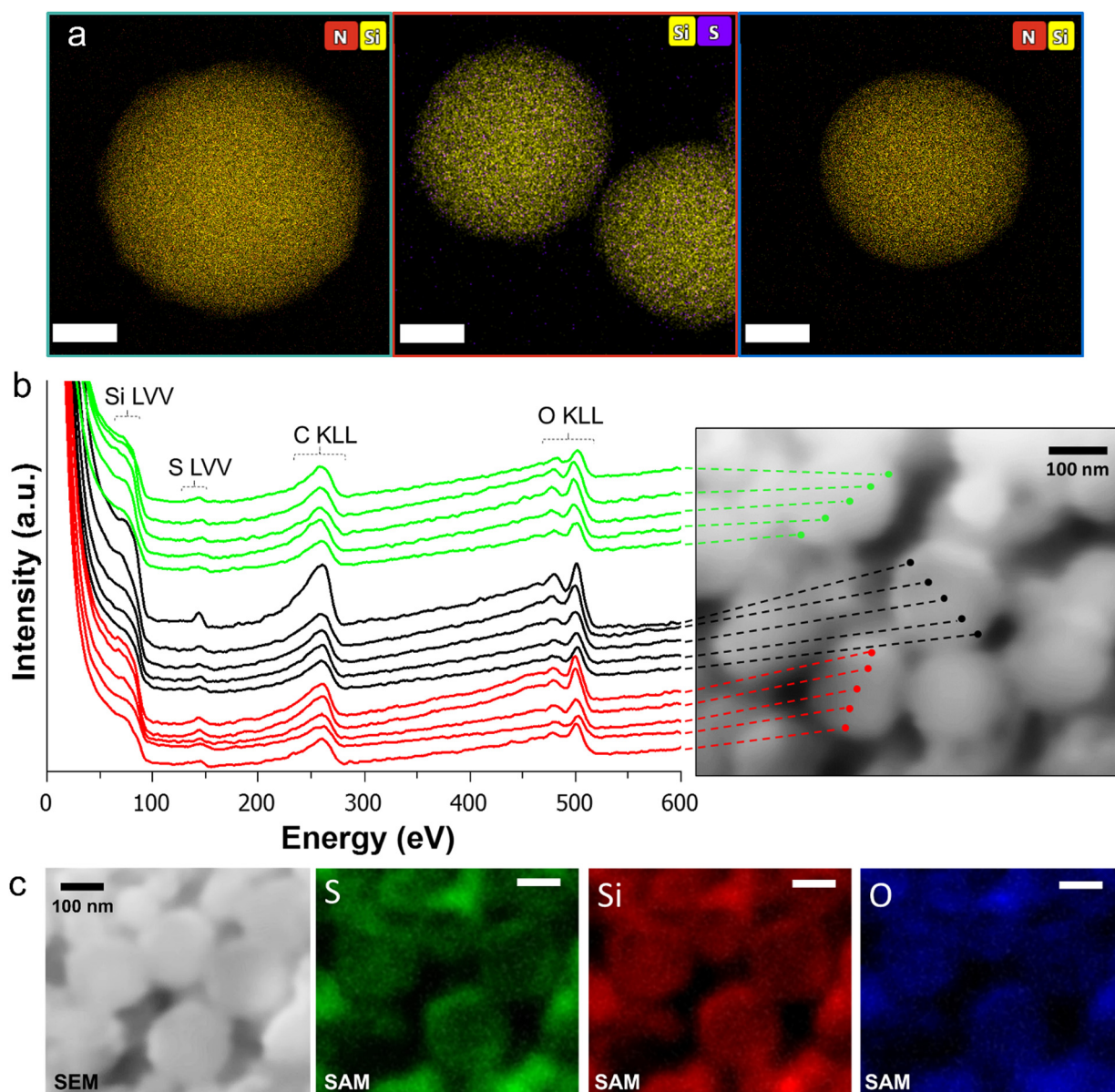

Fig. 4 Chemical mapping of the prepared hybrids. (a) EDX TEM mapping of the particles prepared with 30 mol% of CPTES (left), MPTES (middle), and APTES (right). (b) Auger Electron Spectra of three cross-cut particles with the corresponding target dots along the particle sections of a sample prepared with 30 mol% MPTES. (c) Scanning Auger mapping elemental images of S (green), Si (red), and O (blue) within the same sample with the corresponding secondary electron SEM image of the analyzed area.

Fig. S5, ESI†). Interestingly, the systems prepared with CPTES and MPTES show similar intensities of T^n represented by the whole area bellow the curve at ~ -60 ppm, Fig. 3f. The higher signal of the ternary group in the case of APTES is due to a larger incorporation of functional groups within the resulting material.

These experiments allowed us to identify two parameters which appear to influence microporosity, the presence of Q^2, and the geometry around the functional group. When we compare the hybrid materials, CPTES shows the highest microporosity. Both CPTES and MPTES have Q^2 peaks, while TEOS and APTES do not clearly display a Q^2 peak (Fig. S5, ESI†). CPTES exhibits more microporosity despite a similar degree of condensation to MPTES. Thus, we hypothesize that microporosity results from the lower flexibility around the sp^1 carbon, ensuing more difficulty to occupy space within the SiO_2 network.

EDX STEM analysis has been conducted to give information about the elemental distribution of the organic functionality within the particles (Fig. 4a). Despite a low signal from the elements present in the organic functionality, i.e. N and S, particle mapping has been performed. The mapped particles show no difference in the distribution of the functionality, all hybrid materials display homogeneous elemental distribution within the particles. Due the X-ray characteristic depth of escape being about 1 µm, EDX involves in-depth detection of elemental species in the bulk materials. To provide a complete description of the elemental distribution of materials, Auger electron spectroscopy (AES) and scanning Auger mapping (SAM) has been performed to characterize the elemental distribution of the cross-cut particles (Fig. 4b, c and Fig. S6, S7, ESI†) at the nanoscale with spatial and depth resolution of 10 nm and 5 nm respectively.

A cross-section of the hybrid particles was obtained through argon ion polishing, to access the buried interfaces and to probe the elemental distribution of nitrogen and sulfur atoms within the particles. AES spectra were obtained on the 30 mol% samples by focusing the electron beam probe on several target zones across the section of several particles. Concerning MPTES, Si LVV, C KLL, and O KLL Auger transitions were visible, as shown in Fig. 4b. The S LVV transition at 130–155 eV, coming from the thiol functionality, was visible in all three particles analyzed. In order to obtain further information about the sulfur distribution, SAM chemical maps were obtained (Fig. 4c). Sulfur distribution within the particles appears to be relatively homogeneous, with no clear segregation of this element at this level of the spatial resolution ($\approx$ 10 nm). This homogeneous distribution is consistent with an aggregative particle growth mechanism.

Concerning CPTES-based particles, Si LVV (67–100 eV), C KLL (220–284 eV), and O KLL (462–521 eV) Auger transitions were clearly detected (Fig. S6, ESI†), however, the nitrogen transition was not significantly above the baseline. This indicates a high dilution of cyano functional groups within the particles, probably due to a relatively low CPTES loading in comparison to APTES, as is observed in the MAS ^{29}Si NMR and TGA analysis (Fig. 2g and 3f). Thus, the distribution of CPTES

functionality cannot be determined from N, but C analysis indicates homogenous distribution.

For APTES, the same Si, C, and O Auger transitions have been detected. A slight, but significant signal for the N KLL transition is detected at 365–385 eV, corresponding to the amine functional group (Fig. S7, ESI†). The section of three particles was probed and no clear or significant elemental segregation of nitrogen is observed in the spectra at this detection threshold. Thus, all three systems appear to have a homogeneous distribution of their functionalities throughout the silica particles. While the previously reported syntheses of hybrid particles via two-step routes lead to the location of the functionality of interest at the particle external layer, the co-condensation method reported here is an efficient way to prepare particles with homogeneous spatial repartition of the functionality within the particle.

Conclusions

We showed that the co-condensation method is efficient to prepare functional silica hybrids. The methods used show both similarities and differences between the three hybrid systems. In every case, a homogeneous distribution of functionalities is observed within the particles, due to the particle formation mechanism, which is via the aggregation of seed particles. TGA gave preliminary information about the incorporation of organic functionality and the degree of condensation, showing that APTES was incorporated into the silica to a significant degree, but that MPTES and CPTES were more difficult to co-condense with TEOS. The MPTES and CPTES co-condensed particles showed rougher surfaces and increased microporous volume and specific surface area, as measured by nitrogen sorption analysis. We observed that the size of the particles prepared with APTES stay mostly constant with increasing percentage used of organosilane. The other systems exhibit larger sizes but also bimodal size distribution. It thus appears that particles containing cyano- and thiol-functionalities have a lower degree of particle ripening and post-aggregation condensation due to capping the surface hydroxyl groups and a decreased capacity to redissolve the organoalkoxide molecules. This thorough investigation of functional silica hybrid particles prepared by co-condensation of TEOS and selected organoalkoxides reveals that properties such as microporosity, surface charge, size distribution, particle diameter and the degree of condensation can be tuned via the careful choice of organoalkoxide nature and concentration. In addition, the co-condensation method ensures a homogeneous spatial distribution of the chemical functionality within the particle.

Author contributions

The manuscript was written through contributions of all authors. All authors have given approval to the final version of the manuscript. Conceptualization CS and GLD; formal analysis FB, CCN, PSC, JA and CB; funding acquisition CS

This journal is © The Royal Society of Chemistry 2025

J. Mater. Chem. C, 2025, **13**, 7318–7326 | **7325**

and GLD; investigation FB, SL, ED, JBL; methodology FB, CCN, CS and GLD; project administration GLD; supervision CCN, CS and GLD.

Data availability

Data for this article, including quantification of the hybrid content in silica by TGA, particle diameters, pore size analysis, micrographs, elemental analysis, and the NMR analysis are available at Zenodo at **https://doi.org/10.5281/zenodo.14604913**.

Conflicts of interest

There are no conflict of interest to declare.

Acknowledgements

Notes and references

1 D. Shen, J. Yang, X. Li, L. Zhou, R. Zhang, W. Li, L. Chen, R. Wang, F. Zhang and D. Zhao, *Nano Lett.*, 2014, **14**, 923–932.

2 W. Gao, M. Rigout and H. Owens, *J. Nanopart. Res.*, 2016, **18**, 387.

3 E. Rusak, I. Staude, M. Decker, J. Sautter, A. E. Miroshnichenko, D. A. Powell, D. N. Neshev and Y. S. Kivshar, *Appl. Phys. Lett.*, 2014, **105**, 221109.

4 L. Yang, T. Hu, A. Shen, C. Pei, B. Yang, T. Dai, H. Yu, Y. Li, X. Jiang and J. Yang, *Opt. Lett.*, 2014, **39**, 1909.

5 D. A. Kurdyukov, D. A. Eurov, D. A. Kirilenko, V. V. Sokolov and V. G. Golubev, *Microporous Mesoporous Mater.*, 2018, **258**, 205–210.

6 I. A. Rahman, M. Jafarzadeh and C. S. Sipaut, *Ceram. Int.*, 2009, **35**, 1883–1888.

7 E. Péré, H. Cardy, V. Latour and S. Lacombe, *J. Colloid Interface Sci.*, 2005, **281**, 410–416.

8 J. Lin, H. Chen, Y. Ji and Y. Zhang, *Colloids Surf., A*, 2012, **411**, 111–121.

9 T. Matsoukas and E. Gulari, *J. Colloid Interface Sci.*, 1988, **124**, 252–261.

10 A. van Blaaderen and A. Vrij, *J. Colloid Interface Sci.*, 1993, **156**, 1–18.

11 J. Mosquera, I. García, M. Henriksen-Lacey, G. González-Rubio and L. M. Liz-Marzán, *Chem. Mater.*, 2019, **31**, 57–61.

12 J. Li, L. Chen, Z. Wen, Z. Zhang, J. Luo, C. Yu and P. Wang, *IOP Conf. Ser.:Mater. Sci. Eng.*, 2018, **382**, 022077.

13 J. P. Gonçalves, D. Promlok, T. Ivanov, S. Tao, T. Rheinberger, S. Jo, Y. Yu, R. Graf, M. Wagner, D. Crespy, F. R. Wurm, L. Caire Da Silva, S. Jiang and K. Landfester, *Angew. Chem., Int. Ed.*, 2023, **62**, e202216966.

14 H. Zhang, J. Zhang, C. Wu, B. Zhang and Q. Zhang, *Silicon*, 2019, **11**, 2819–2827.

15 H. Zou and Y. Ren, *Nanoscale*, 2023, **15**, 10484–10497.

16 J. Kusz, C. Boissiere, Y. Bretonnière, C. Sanchez and S. Parola, *Nanoscale*, 2024, **16**, 18918–18932.

17 J. Kusz, C. Boissiere, D. Ihiawakrim, O. Ersen, C. Sanchez and S. Parola, *Chem. Mater.*, 2023, **35**, 7671–7682.

18 A. Roghanizad, M. Karimi Abdolmaleki, S. M. Ghoreishi and M. Dinari, *J. Mol. Liq.*, 2020, **300**, 112367.

19 J. Ciccione, T. Jia, J.-L. Coll, K. Parra, M. Amblard, S. Jebors, J. Martinez, A. Mehdi and G. Subra, *Chem. Mater.*, 2016, **28**, 885–889.

20 M. Marini, B. Pourabbas, F. Pilati and P. Fabbri, *Colloids Surf., A*, 2008, **317**, 473–481.

21 C. H. Lee, S. H. Park, W. Chung, J. Y. Kim and S. H. Kim, *Colloids Surf., A*, 2011, **384**, 318–322.

22 J. H. Shin, S. K. Metzger and M. H. Schoenfisch, *J. Am. Chem. Soc.*, 2007, **129**, 4612–4619.

23 A. A. Issa and A. S. Luyt, *Polymers*, 2019, **11**, 537.

24 M.-C. Brochier Salon, P.-A. Bayle, M. Abdelmouleh, S. Boufi and M. N. Belgacem, *Colloids Surf., A*, 2008, **312**, 83–91.

25 S.-L. Chen, P. Dong, G.-H. Yang and J.-J. Yang, *Ind. Eng. Chem. Res.*, 1996, **35**, 4487–4493.

26 M. G. Voronkov, Iu. A. IUzhelevsk'ii and V. P. Mileshkevich, *The siloxane bond: physical properties and chemical transformations*, Consultants Bureau, 1978.

27 M.-C. Brochier Salon and M. N. Belgacem, *Colloids Surf., A*, 2010, **366**, 147–154.

28 M. Szekeres, J. Tóth and I. Dékány, *Langmuir*, 2002, **18**, 2678–2685.

29 G. H. Bogush and C. F. Zukoski, *J. Colloid Interface Sci.*, 1991, **142**, 1–18.

30 F. Kunc, V. Balhara, Y. Sun, M. Daroszewska, Z. J. Jakubek, M. Hill, A. Brinkmann and L. J. Johnston, *Analyst*, 2019, **144**, 5589–5599.

31 R. J. Oliveira, J. F. De Conto, M. R. Oliveira, S. M. S. Egues, G. R. Borges, C. Dariva and E. Franceschi, *J. CO2 Util.*, 2019, **32**, 232–240.

32 P. López-Aranguren, J. Fraile, L. F. Vega and C. Domingo, *J. Supercrit. Fluids*, 2014, **85**, 68–80.

33 M. Kosmulskis and E. Matijevib, *Langmuir*, 1992, **8**, 1060–1064.

34 Z. Wu, H. Xiang, T. Kim, M.-S. Chun and K. Lee, *J. Colloid Interface Sci.*, 2006, **304**, 119–124.

35 A. Lecloux, J. Bronckart and F. Noville, *Colloids Surf.*, 1986, **19**, 359.

7326 | *J. Mater. Chem. C*, 2025, **13**, 7318–7326

This journal is © The Royal Society of Chemistry 2025